https://doi.org/10.5194/essd-2026-566
Preprint. Discussion started: 28 July 2026

Open Access Earth System Science Data Discussions

GLOBESINK: A global climatology of sinking organic carbon flux and particle size from optical backscattering measurements.

Nathan Briggs[1], Stephanie Henson[1], Anita Flohr[1], Hans Hilder[1]

[1]National Oceanography Centre, Southampton, UK

Correspondence to: Nathan Briggs (natbrig@noc.ac.uk)

Abstract. Sinking particles play a major role in the global carbon cycle, driving long-term carbon storage in the ocean and providing the primary food source for many deep ocean ecosystems. However, the global flux of sinking organic matter to the deep ocean is poorly constrained, due to the difficulty of measuring sinking particles at global scale. Here we present a global, gridded monthly climatology of size-fractionated optical backscattering by particles ranging from 1-800 µm, derived from the Biogeochemical Argo network of profiling floats. We leverage these data to estimate particulate organic carbon (POC) concentrations and sinking fluxes, as well as area-weighted mean particle diameter and the number concentrations of particles in three size classes: 200-400 µm, 400-800 µm, and >800µm. Each estimate of carbon concentration and flux is accompanied by an estimate of uncertainty due to the empirical relationships used to convert from backscatter, and each quantity derived from backscattering from one or more large (>200 µm) size class is accompanied by an estimate of precision due to random encounter with rare, large particles. For reference, climatologies of the following other parameters measured by the same floats are included: temperature, salinity, nitrate, pH, oxygen, and Chlorophyll a concentration. All climatologies share the same regular grid, with 4° latitude by 8° longitude resolution and spanning 0-2000 m depth, with vertical resolution varying from 10 m to 300 m. The raw climatology, containing gaps in the months, coordinates, and depths without data, is accompanied by a spatially smoothed and interpolated climatology that fills in these gaps, except for the Arctic and areas of near-permanent sea ice around Antarctica. The estimates of POC concentration and particle size are presented as is, without validation, but the estimates of sinking POC flux were validated against a global dataset of independent measurements, finding a mean relative bias of 1.2 and an r^2 of 0.57 on a logarithmic scale.

1 Introduction

The downward sinking flux of organic matter is a key part of the global carbon cycle. This flux reduces atmospheric CO_2 concentrations by >150 ppm relative to pre-industrial conditions (Tjiputra et al., 2025) while also providing the primary food source for deep ocean ecosystems (Iken et al., 2001; Romero-Romero et al., 2021). The strength of this downward flux is expected to change as the oceans warm, but the magnitude and even direction of this change is still uncertain (Canadell et al., 2021). A key limiter of progress in predictive understanding is the sparseness and uncertainty of sinking particulate organic carbon (POC) flux measurements. Traditional measurements of POC flux, from sediment traps and thorium-234 disequilibria,

https://doi.org/10.5194/essd-2026-566
Preprint. Discussion started: 28 July 2026

require sample collection from ships and/or moorings, which is currently not practical to make at the global, seasonally-resolved scale necessary to constrain global models (Lima et al., 2014). Furthermore, POC fluxes measured by different methods often disagree by a factor of 2 or more due to a range of methodological biases, making patterns in current measurements from different regions and seasons difficult to interpret (Buesseler and Boyd, 2009; Usbeck et al., 2003; Baker et al., 2020).

Several methods have been proposed to improve the spatial and temporal coverage of POC flux measurements. A range of satellite ocean colour-based methods have been developed to estimate the export flux of POC from the surface ocean (Henson et al., 2011; Siegel et al., 2014). However, satellites cannot directly measure sinking particles nor their attenuation with depth, so these methods must rely on empirical and/or foodweb models to estimate fluxes from surface properties such as chlorophyll concentration. Therefore, while extremely valuable as a check on model spatial and seasonal patterns, their power to independently constrain models of flux to depth is still limited. Several in-situ optical techniques have been developed that derive POC flux from more direct, depth-resolved measurements of sinking particles that can in principle be made at global scale from autonomous platforms. These techniques include in-situ imagery (Guidi et al., 2015), use of a beam transmissometer as an optical particle collector (Bishop et al., 2004; Estapa et al., 2019), and use of transient "spikes" in optical backscattering measurements to detect large particles and their bulk sinking speed (Briggs et al., 2011; Henson et al., 2023; Briggs et al., 2020). Optical backscattering is the first of these in-situ optical measurements to achieve global, year-round coverage, due to recent expansion of the Biogeochemical Argo network of autonomous profiling floats (Roemmich et al., 2019; Claustre et al., 2020), which now covers all ocean basins except the Arctic.

Here we present a new, gridded global monthly climatology of sinking POC flux due to particles <800 µm between the surface and 2000 m depth derived by adaptation of the "optical backscattering spikes" particle size fractionation method (Briggs et al., 2011; Briggs et al., 2020). The approach has been applied to the entire backscattering dataset collected by the Biogeochemical Argo float network from 2010 through May 2025. This climatology includes central estimates derived from parameters chosen for agreement with a global database of traditional flux measurements, as well as upper and lower bounds derived from propagated random and systematic uncertainties. Alongside these POC flux estimates, we include a range of other related measurements on the same grid, derived from the same floats: temperature, salinity, pH, optical backscattering, downwelling photosynthetically available radiation, area-weighted mean particle diameter, concentrations of particles in three size classes, and concentrations of chlorophyll a, dissolved oxygen, and nitrate. We anticipate that this dataset will provide a valuable new independent constraint on the global flux of organic carbon to the deep ocean and the drivers of its variability in space and time.

https://doi.org/10.5194/essd-2026-566
Preprint. Discussion started: 28 July 2026

2 Methods

2.1 Data source

All data were downloaded from the ftp site of the Coriolis Global Data Assembly Center: ftp.ifremer.fr/ifremer/argo/dac/. The Argo synthetic file index was used to find all Argo profiles containing measurements of temperature (T), salinity (S), particulate optical backscattering (b_{bp}), and chlorophyll a fluorescence (F_{Chl}) measurements between Jan 1, 2010 and May 31, 2025.

2.2 Automated QC

2.2.1 Initial spike filter

A five-point running median was used to separate each profile of b_{bp} into a low-frequency baseline b_{brs_med} and a high-frequency "spike" signal ($b_{bl\_med\_raw}$). See Table 1 for definitions of b_{bp} partitions.

2.2.2 Initial range test

High and low backscattering outliers were identified using the following procedures. Median filtered backscatter data (b_{brs_med}) were first filtered using a depth-dependent range test to remove values deemed to be outside the expected open-ocean range, using the following depth-dependent thresholds, set visually to identify clear outliers within the global Argo dataset. Data with b_{brs_med} >0.03 m^{-1} were excluded at all depths. Data with b_{brs_med} >0.004 m^{-1} were excluded for depths greater than 200 m. Data with b_{bp}>0.002 m^{-1} were excluded for depths greater than 500 m.

2.2.3 Depth Binning For QC

After the removal of b_{brs_med} data failing the range test, each profile was divided into vertical bins with the following spacing: 10 m between 0 and 250 m, 25 m between 250 and 425 m, 50 m between 425 and 1025 m, and 100 m between 1025 and 2025 m. For each bin, the median b_{brs_med} was calculated (b_{brs_binned}). Depth bins were then smoothed temporally using a three-point running median (i.e. 30 days for typical BGC-Argo sampling) to remove single profile outliers, yielding $b_{brs\_binned\_smoothed}$.

2.2.4 Detection of local outliers

Positive and negative outliers were determined from a combination of local variability and measurement resolution. For each float, the minimum resolution r_{bbp} was determined as the 0.3 quantile of the absolute value of differences between consecutive measurements of unbinned, unsmoothed b_{bp}. For each data point of b_{brs_binned}, the surrounding local variability was characterised by calculating quantiles $Q_{0.05}$, $Q_{0.5}$, and $Q_{0.95}$ of $b_{brs\_binned\_smoothed}$ within a 9x9 window (±4 profiles and ±4 depth bins). Quantiles were only calculated for windows containing data in at least 36 out of the maximum 81 bins in the 9x9 surrounding bins. Missing data could be caused by several factors, including proximity to the shallowest or deepest bins, failure of the initial

https://doi.org/10.5194/essd-2026-566
Preprint. Discussion started: 28 July 2026

Open Access Earth System Science Data Discussions

range test, or shallow profiles due to either bathymetry or custom profiling strategies. Gaps were then filled in the quantiles via nearest neighbor interpolation. Positive and negative outliers were determined from the gap-filled moving $b_{brs\_binned\_smoothed}$ quantiles via the following thresholds.

Positive outliers: $b_{brs\_med} > Q_{0.95} + \max[(Q_{0.95} - Q_{0.5})*1.8, [(Q_{0.95} - Q_{0.05})*0.9] + r_{bbp}*5$

Negative outliers: $b_{brs\_med} < Q_{0.05} - (Q_{0.5} - Q_{0.05})*1.8) - r_{bbp}*5$

Note that quantiles $Q_{0.05}$, $Q_{0.5}$, and $Q_{0.95}$ were calculated on the smoothed, gap-filled, binned data, but outliers were identified on individual b_{brs_med} datapoints, which were not binned or temporally smoothed.

2.2.5 Automated removal of bad data

All negative and positive outliers identified via the thresholds above were removed from further processing. In addition, any datapoint within 80 m of a positive outlier identified on a given profile was removed. Removed data are not included in the data product. See Figs. 1-3 for examples of automated data removal.

2.3 Size partitioning and per-profile binning

2.3.1 Size partitioning of b_{bp}

The b_{bp} signal was partitioned into five fractions: $b_{bp} = b_{br} + b_{bs} + b_{bm} + b_{bl} + b_{bx}$, corresponding to “refractory”, “small”, “medium”, “large”, and “extra large.” Details are shown in Table 1. Two different statistical filters were used to partition the small refractory and labile signal b_{brs} from the larger fractions. The first was the 5-point running median described in section 2.2.1, which separated b_{bp} into b_{brs_med} and $b_{bml\_med\_raw}$. In addition to its use in automated quality control, this filter was used in calculation of mean particle diameter (see section 2.8). The second statistical filter, used for the POC flux estimations, was a 5-point running minimum followed by a 5-point running maximum, which separated b_{bp} into two initial size fractions b_{brs} and b_{bml_raw}. b_{brs} is a more conservative estimate than b_{brs_med}, because the “min-max” filter more robustly separates higher concentrations of large particles from a background free of large particles when small-particle concentration is constant or changing monotonically with depth. On the other hand, subsurface peaks in small-particle b_{bp} will also contribute to b_{bml_raw}. It is therefore most appropriate to use the min-max filter in the mesopelagic.

Within the mesopelagic, b_{bml_raw} can over-estimate large- and medium-particle b_{bp} for two additional reasons. First, sensor noise contributes to b_{bml_raw}. Second, swimming animals, generally larger than 1 mm, are sometimes attracted to the b_{bp} sensor (Haentjens et al., 2020), causing large numbers of b_{bp} spikes which are not due to sinking particles. In order to reduce these sources of error and standardise our “large- and medium-particle” signals, we then separated b_{bml_raw} into four fractions using spike height thresholds: $b_{bml\_raw} = b_{b\_noise} + b_{bm} + b_{bl} + b_{bx}$, where b_{b_noise} includes spikes due to instrument noise as well as some particles <200 µm, b_{bm} is the contribution to b_{bp} of particles between 200 and 400 µm, b_{bl} is the contribution of particles between 400 and 800 µm, and b_{bx} the contribution of particles >800 µm. The thresholds of b_{bp} corresponding to these diameters

https://doi.org/10.5194/essd-2026-566
Preprint. Discussion started: 28 July 2026

were converted into equivalent b_{bml_raw} values assuming each "spike" is caused by a single particle. The conversion was made following (Briggs et al., 2013), assuming a backscattering efficiency Q_{bb} of 0.024 and sample volume V_{bb} of 10 ml (Briggs et al., 2020). Using this conversion, the thresholds of 200, 400, and 800 µm correspond to b_{bml_raw} values of $1x10^{-4}$ m^{-1}, $4x10^{-4}$ m^{-1}, and $16x10^{-4}$ m^{-1}, respectively. Therefore, b_{bm} was obtained from b_{bml_raw} by setting all values of b_{bml_raw} less than $1x10^{-4}$ m^{-1} or greater than $8x10^{-4}$ m^{-1} equal to zero. We similarly obtained b_{bl} and b_{bx} from b_{bml_raw} by setting all values outside their respective thresholds to zero. Because b_{bl_med} is not biased by random, evenly-distributed instrument noise, it was partitioned in a similar way but only into two fractions: $b_{bml\_med\_raw} = b_{bml\_med} + b_{bx\_med}$. The partitioning of small-particle signal b_{brs} into a refractory pool b_{br} and a labile pool b_{bs} is detailed below in section 2.7.

2.3.2 Particle number concentrations from b_{bl}

The assumptions in the previous section also allow us to calculate particle number concentration. Each nonzero value of b_{bm}, b_{bl}, or b_{bx} represents a single observation of a particle of the corresponding size (200-400µm, 400-800µm, or >800µm). For a given series of b_{bp} measurements, number concentrations in these size classes C(200-400µm), C(400-800µm), and C(>800µm) are simply the number of nonzero b_{bm}, b_{bl}, or b_{bx} measurements, respectively divided by the total volume sampled, given as V_{bb} times the number of observations. While these number concentrations are not used in the flux calculations, they are included in the GLOBESINK dataset for reference.

Table 1. Partitioning of b_{bp}

Abbreviation	Approximate size range in equivalent spherical diameter	Description
b_{br}	ESD < 200 µm	"Refractory" backscattering signal. Seasonally and vertically invariant local "blank"
b_{bs}	ESD < 200 µm	Small, slow-sinking, labile particles
b_{bm}	200 µm < ESD < 400 µm	Medium-sized labile particles
b_{bl}	400 µm < ESD < 800 µm	Large, fast-sinking, labile particles
b_{bx}	ESD > 800 µm	Particles too large and rare to include in flux calculations. Includes signal of zooplankton attracted to the sensor.
b_{brs}	ESD < 200 µm	bbr + bbs
b_{bml}	200 µm < ESD < 800 µm	bbm + bbl
_med		Suffix for size partition using median filter
_raw		Suffix for preliminary large-particle fraction obtained from raw spike signal filter

https://doi.org/10.5194/essd-2026-566
Preprint. Discussion started: 28 July 2026

_noise		Suffix for fraction of b_{bml_raw} attributed to instrument noise and/or particles < 200 µm

2.3.3 Vertical binning

Each float profile was divided into vertical bins with boundaries at the following depths: 0 m, 10 m, every 50 m from 50 to 900 m, 1000 m, every 200 m from 1200 to 1800 m, and 2100 m. These depths were chosen to isolate the upper 10 m, where surface effects including bubbles can contribute to b_{bp}. For each bin, the mean of all parameters was calculated. In addition, the standard deviations of both b_{bl_med} and $b_{bl\_med\_raw}$ were calculated, and the number of b_{bp} data points saw also counted, after removal of data due to quality control. In addition to b_{bp} and derived parameters, all other standard available BGC Argo parameters were bin averaged. Because the automated QC procedure detailed in Section 2.2.4 requires a 9-profile running window, only floats with at least 9 profiles were used for further analysis.

2.3.4 Removal of shallow bathymetry

To reduce signals from re-suspended sediments, version 2.0 of the GEBCO one-minute bathymetric grid was used to find the shallowest bottom depth within 10 km horizontally of each profile. If this nearby bottom depth was shallower than 300 m, the entire profile was removed from the dataset. If the nearby bottom depth was deeper than 300 m, any bins fewer than 200 m above this depth were removed from the dataset.

2.4 Visual QC

For each float, both raw and binned b_{brs} and b_{bml_raw} data were plotted as a function of time and depth, both with and without automated QC. Profiles were screened for six types of error, listed in Table 2, each associated with a QC flag. QC1: Brief increases in b_{brs} at all depths (“stripy profiles”), suggestive of temporary fouling. QC2: Brief increases in b_{bml_raw} at all depths, suggestive of temporary fouling. QC3: Gradual increase in b_{brs} at all depths suggesting cumulative biofouling. QC4: Elevated b_{brs} and/or b_{bml_raw} associated with shallow bathymetry, suggesting possible re-suspended sediments. QC5: Elevated b_{brs} and/or b_{bml_raw} at bottom of profile, suggesting resuspension of particles that had settled on float during drift period. QC6: b_{brs} too low (negative or visually unrealistic negative anomaly). Profiles flagged with any of the visual QC flags were removed from further analysis. Examples of data removal due to these visual QC flags are shown in Figs. 1-3.

Table 2: Visual QC flags on the depth-binned profiles after automated QC.

QC flag	Criteria	# of profiles removed (# of floats with at least 1 profile removed)	# of floats removed entirely
1	stripy profiles in baseline	555 (46)	6

https://doi.org/10.5194/essd-2026-566
Preprint. Discussion started: 28 July 2026

2	stripy profiles in spikes	98 (9)	1
3	signs of gradual fouling	790 (11)	26
4	bathymetry, potential resuspended sediment impact or too shallow profiling	1377 (28)	44
5	high surface production, spikes at max depth, particles settled on float?	216 (3)	2
6	b_{brs} too low	317 (9)	7
	total	3353	86

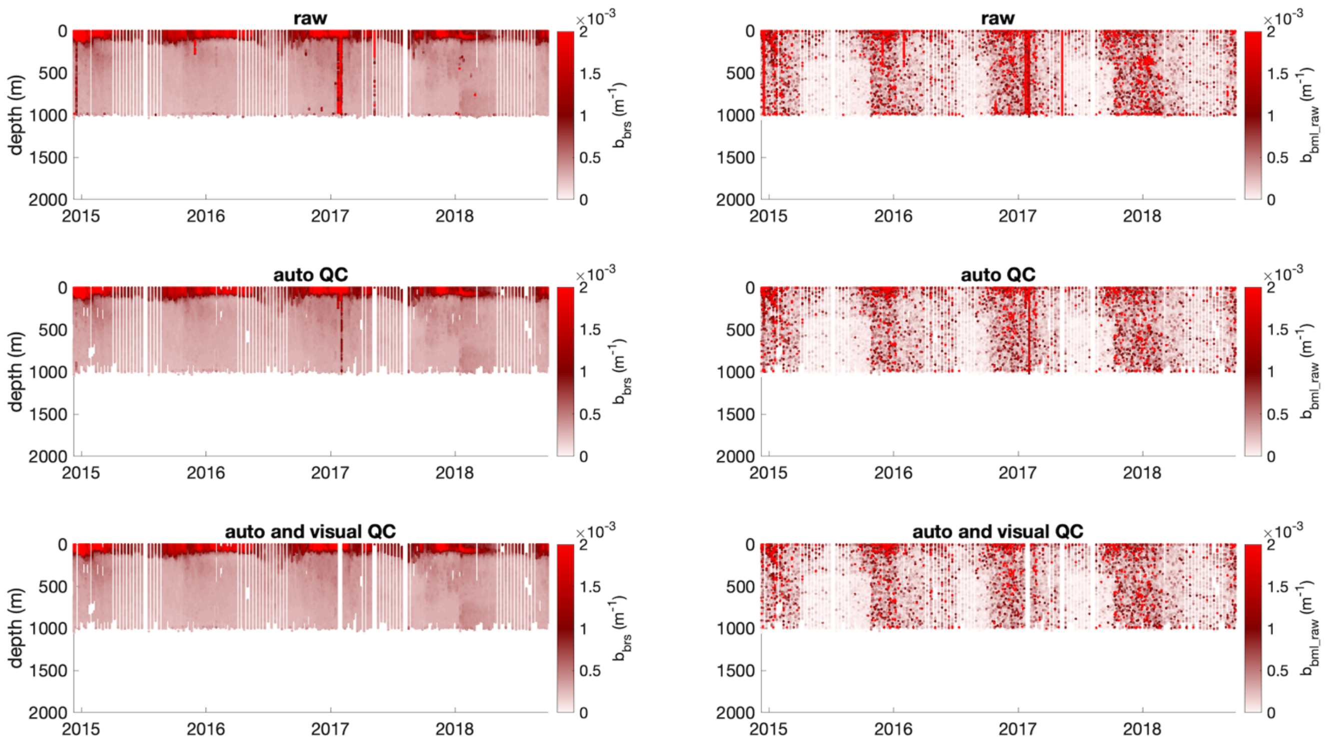

Figure 1. Example of visual QC flags 1 and 2 (WMO6901582) – "stripy" profiles. Left column shows (top to bottom), raw b_{bs}, b_{bs} after automated QC is applied and b_{bs} after both automated and visual QC is applied. Right column shows the same but for b_{bl}.

https://doi.org/10.5194/essd-2026-566
Preprint. Discussion started: 28 July 2026

Open Access Earth System Science Data Discussions

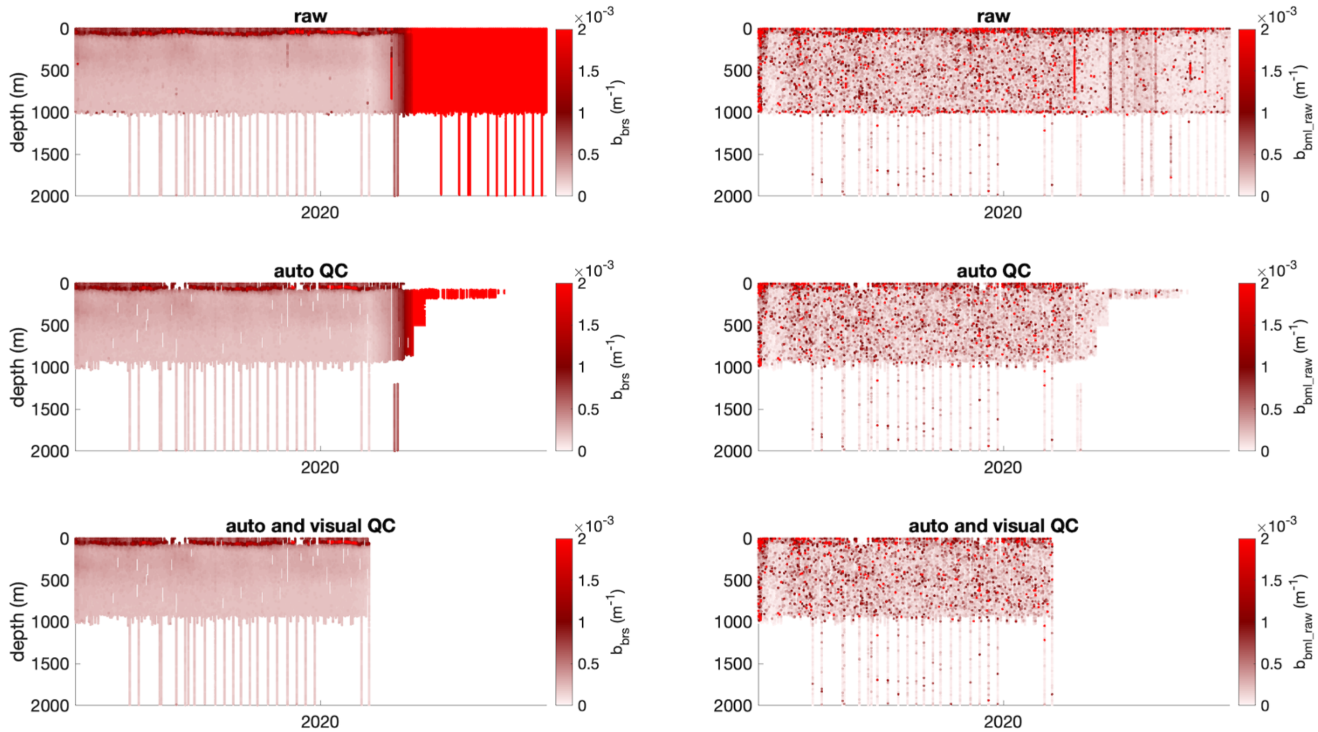

Figure 2. Example of visual QC flag 3 (WMO3902122) – start of gradual fouling. Left column shows (top to bottom), raw b_{bs}, b_{bs} after automated QC is applied and b_{bs} after both automated and visual QC is applied. Right column shows the same but for b_{bl}.

https://doi.org/10.5194/essd-2026-566
Preprint. Discussion started: 28 July 2026

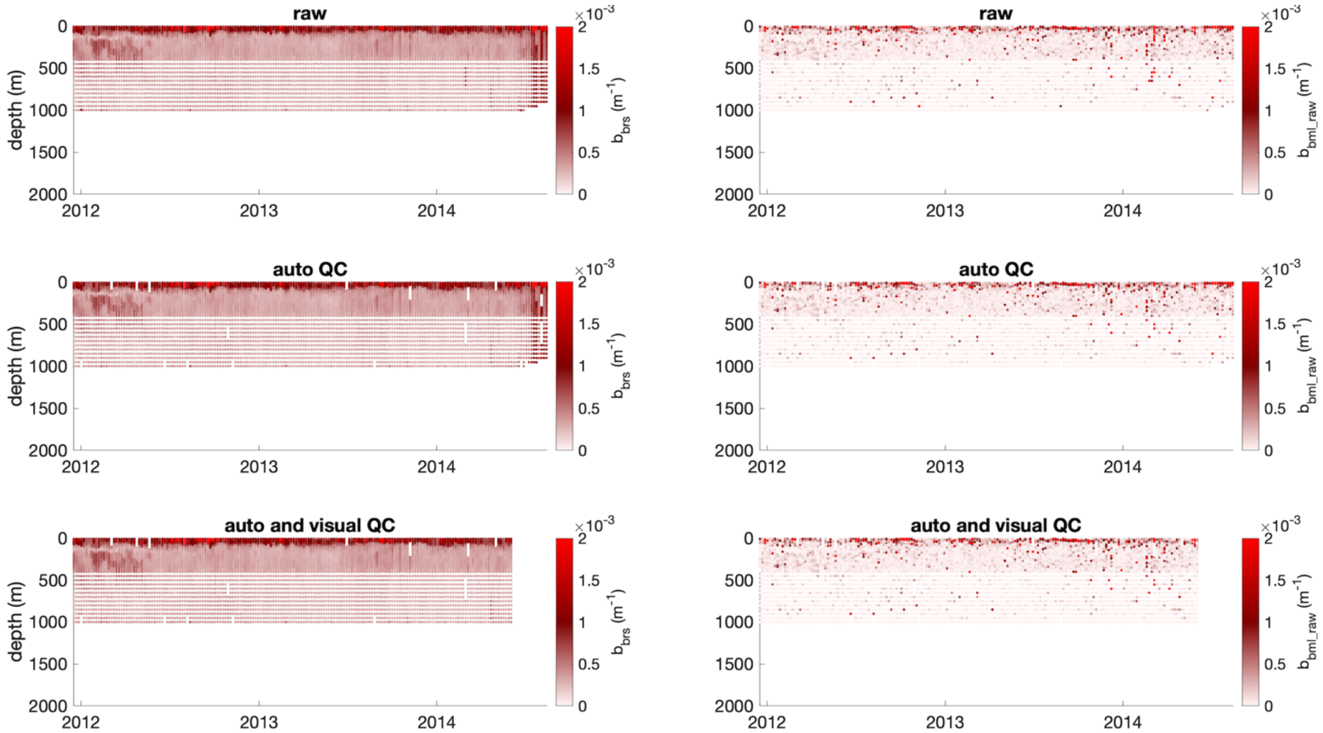

Figure 3. Example of visual QC flags 1 and 4 (WMO5903586) – "stripy profiles" and potential resuspension. Left column shows (top to bottom), raw b_{bs}, b_{bs} after automated QC is applied and b_{bs} after both automated and visual QC is applied. Right column shows the same but for b_{bl}.

2.5 Monthly binning

For each float, per-profile vertical bins were combined into monthly bins, using the mean value weighted by the sample number. The binned b_{brs} data were then aligned with nearby floats at depth as explained in the next section. The monthly bins were then gridded into a global monthly climatology, using a 4° latitude by 8° longitude grid, chosen to balance precision with resolution. The gridded products again used the mean, weighted by sample number. This weighting is most important for the large-particle b_{bp} products, because these quantities rely on random encounters with rare particles.

2.6 Alignment of deep b_{bp}

Systematic offsets in mesopelagic b_{brs} were observed between nearby floats in some regions, leading the global gridded dataset to appear noisy at depth. These differences include initial sensor calibration uncertainty as well as possible changes to sensor performance upon integration and deployment. To reduce spatial and seasonal noise introduced by these offsets, we characterised and corrected them using the following steps.

https://doi.org/10.5194/essd-2026-566
Preprint. Discussion started: 28 July 2026

1. For each monthly-averaged float timeseries, each monthly b_{brs} profile was matched with all other monthly-averaged b_{brs} profiles from other floats (profiling to at least 425 m depth) whose mean location was within 2000 km of the primary float in the same month of the year. Note that matchups do not need to be from the same year.
2. For each secondary float that matched up with the primary float in at least one month, the difference in b_{brs} between the two floats was calculated at three deep reference depths: 425 m, 940 m, and 1750 m. The deep offset between the primary and secondary float was defined as the median difference across all three depths (secondary minus primary).
3. For each primary float, a single "alignment offset" was calculated as the median of all deep offsets calculated in step 2.
4. Each float's entire b_{brs} timeseries was adjusted by half of the alignment offset from step 3. This is to allow floats that matched with only one other float to "meet in the middle".
5. Steps 2-4 were repeated on the partially-aligned float data, this time subtracting the full remaining alignment offset.

A list of the final alignment offsets for each float is published alongside the GLOBESINK dataset. The dataset itself contains only post-alignment data.

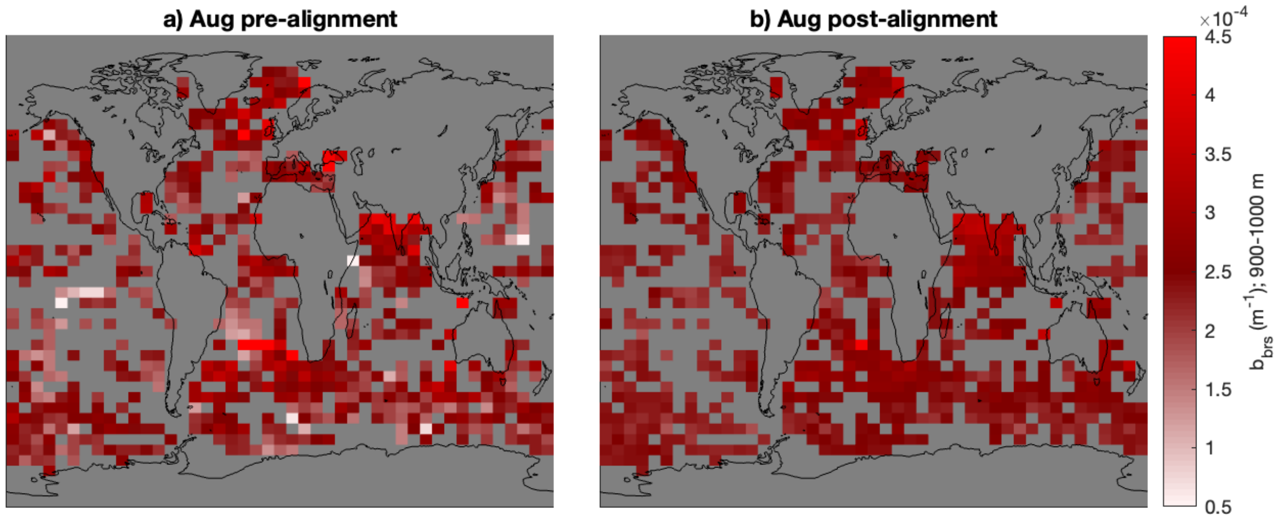

Figure 4. Deep b_{brs} before (a) and after (b) alignment of nearby floats.

2.7 Partitioning of refractory and labile small-particle b_{bp}

The contribution to b_{bp} by a hypothesized time- and depth-invariant pool of small, refractory particles was estimated as follows from the 8° by 4° gridded monthly climatologies of b_{brs}. First, the gridded climatologies were smoothed using a 3x3 pixel moving median. Second, gaps were filled via linear interpolation between pixels, so that all pixels contained data for all months. Finally, for each 8° by 4° pixel, b_{br} was defined as the minimum smoothed interpolated climatological b_{brs} across all depths and months. Note that spatial patterns include both variability in concentration of small, refractory particles and any systematic

https://doi.org/10.5194/essd-2026-566
Preprint. Discussion started: 28 July 2026

regional offsets in calibration. Labile small-particle backscattering b_{bs} was calculated as b_{brs}-b_{br}. In rare cases when smoothed b_{br} exceeded b_{brs}, yielding a negative difference, b_{bs} was set to zero.

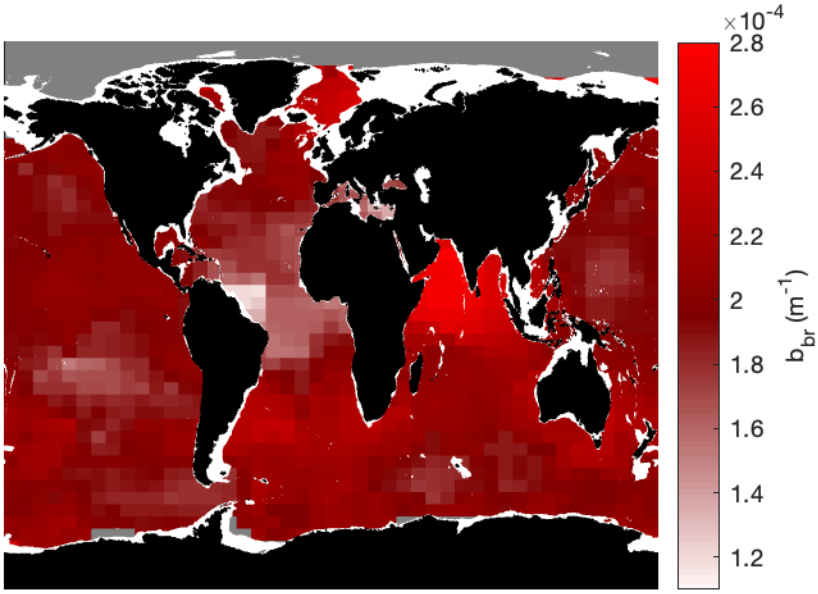

Figure 5. Global map of small, refractory backscattering b_{br}. Treated as a regional blank and not used in POC calculation.

2.8 Area-weighted mean particle diameter

Area-weighted mean particle equivalent spherical diameter of particles <800 µm ($\overline{D}$) was calculated for each bin following (Briggs et al., 2013), via Eq. (1). Specifically, the variance of b_{bml_med} was divided by the mean of b_{brs_med}+b_{bml_med} to obtain the average per-particle b_{bp} including all particles with ESD ≤ 800 µm. A single-measurement sample volume V_{bb} = 10 ml was used as mentioned in Section 2.3.1 based on a sample duration of 1 s and a particle residence time of 0.063 s, derived from a platform vertical velocity of 10 cm s^{-1} and a mean path length of 6.3 mm of particles through the sample volume. Note that this metric has not been quantitatively validated in situ, so it should be treated as indicative.

$$\overline{D} = \sqrt{\frac{4}{\pi}\frac{var[b_{bml\_med}]}{mean[b_{brs\_med} + b_{bml\_med}]}\frac{V_{bb}}{Q_{bb}}} \tag{1}$$

2.9 Estimation of POC flux

2.9.1 Estimation of POC concentration from b_{bp}

To estimate gravitational flux of POC, only b_{bl}, b_{bm}, and b_{bs} were considered, meaning that flux from particles >800 µm in diameter is not included in these estimates (see size fractions in Table 1). Optical backscattering size fractions b_{bl}, b_{bm}, and b_{bs}

https://doi.org/10.5194/essd-2026-566
Preprint. Discussion started: 28 July 2026

were first converted into POC estimates POC_l, POC_m and POC_s, using a depth-dependent POC/b_{bp} ratio that was linear in the top 100 m and a power law deeper than 100 m:

$$POC/b_{bp}(z \leq 100[m]) = 43000\,[mg\;m^{-2}] - 114z[m] \tag{2}$$

$$POC/b_{bp}(z > 100[m]) = 31600[mg\;m^{-2}]\left({}^{z}/_{100[m]}\right)^{-0.45} \tag{3}$$

The upper 100 m relationship was obtained from a reanalysis of the POC and b_{bp} data presented in (Cetinić et al., 2012). We first converted b_{bp} data from this study to b_{bs} as described above, using our estimate b_{br} for the site of this study (western Iceland Basin), which is 0.0002 m^{-1} (see Figure 5). Then linear least-squared regressions were calculated between b_{bs} and POC in five different depth bins, centered at 8, 21, 31, 63, and 101 m. Regressions were forced through the origin, so that each regression produced a single POC/b_{bp} slope and no offset. A linear regression between the five POC/b_{bp} slopes and depth was then calculated to obtain Eq. (2). The multiplier of Eq. (3) was set at 31600 mg m^{-2} to be continuous with Eq. (2) at 100 m. The exponent of Eq. (3) was obtained from a power-law fit to the ratio of POC flux to mass flux data from a global compilation of sediment trap data (Mouw et al., 2016), similar to (Briggs et al., 2011). Total b_{bp}-derived POC is defined as $POC_{bb} = POC_s + POC_m + POC_l$. Upper and lower uncertainty bounds of POC/b_{bp} at 100 m (Table 3) were estimated using a range of published open-ocean near-surface POC/b_{bp} linear regression slopes, normalised to the mean upper-ocean value of 35400 mg m^{-2} of (Cetinić et al., 2012). The highest (Stramski et al., 2008) is a factor of 1.66 higher than (Cetinić et al., 2012) after multiplying by 1.1 to adjust for differing b_{bp} wavelength (Cetinić et al., 2012). The lowest (Johnson et al., 2017) is a factor of 0.88 relative to (Cetinić et al., 2012). Uncertainty bounds for the mesopelagic POC/b_{bp} attenuation coefficient were estimated simply by varying the base estimate of -0.45 by ±50%. While this choice is somewhat arbitrary, it was chosen to reflect high relative uncertainty and ensure that the lower bound includes the value of -0.28 obtained from springtime export of fresh phytodetritus (Briggs et al., 2011).

2.9.2 Estimation of POC flux from size-resolved POC and sinking speed

POC was converted to downward flux using bulk large and small-particle sinking speeds w_l = 74 m d^{-1}, w_m = 48 m d^{-1}, and w_s = 2.5 m d^{-1}. Large-particle sinking speed w_l and uncertainty bounds (see Table 3) were taken from in-situ estimates from 18 high-latitude blooms in the North Atlantic and Southern Ocean (Briggs et al., 2020). Medium particle sinking speed w_m was calculated from w_l based on the global median power-law scaling between marine particle diameter and sinking speed found in (Cael et al., 2021) as

$$w_m = w_l\left(\frac{d_m}{d_l}\right)^{0.63}, \tag{4}$$

where d_m and d_l are the midpoint equivalent spherical diameters of particles contributing to b_{bm} and b_{bl} (300 and 600 µm, respectively). Small-particle sinking speed w_s and uncertainty bounds (2.5±2.5 m d^{-1}) were chosen based on the assumption

https://doi.org/10.5194/essd-2026-566
Preprint. Discussion started: 28 July 2026

that the w_s consists primarily of suspended material ($w_s = 0$), with a minor fraction (0-50%) sinking at 10 m d^{-1} (Briggs et al., 2020).

2.9.3 Systematic Uncertainties

Systematic uncertainties were estimated by propagating uncertainties in key parameters as shown in Table 3. The contribution of each parameter to uncertainty in POC and POC flux was estimated for each bin in time, space, and depth by varying a single parameter between the base value and upper or lower bound and re-calculating POC and POC flux, holding all other parameters at the base value. Single-parameter propagated upper and lower uncertainty intervals were combined quadratically to yield total systematic uncertainty, with an added condition that lower bounds could not be less than zero. Note that while base parameter values were chosen from the literature, choices of which POC/b_{bp} parameters to use for the base value were informed by the validation results described below.

Table 3. Key parameters for POC flux calculation and ranges for uncertainty propagation. Derivation of base values and bounds are described in detail in the text, but key references are noted here.

Parameter	Base value	Lower bound	Upper bound	Units	Notes
w_l	74	58	100	m d^{-1}	(Briggs et al., 2020)
w_m	48	37	65	m d^{-1}	(Briggs et al., 2020; Cael et al., 2021)
w_s	2.5	0	5	m d^{-1}	(Briggs et al., 2020)
POC/b_{bp} at 100 m	31600	27834	52605	mg C m^{-2}	Reanalysis of (Cetinić et al., 2012; Johnson et al., 2017; Stramski et al., 2008)
POC/b_{bp} depth attenuation exponent	-0.45	-0.225	-0.675		Sediment trap POC mass fraction vs. depth from (Mouw et al., 2016)

2.9.4 Precision

Individual estimates of mean particle diameter, large-particle concentration and derived fluxes have inherently poor precision, due to the low sample volume of single float b_{bp} measurements: ~10 ml after accounting for 1 s integration time and 10 cm/s ascent speed. The distribution of b_{bp} measurements within such a small sample volume is highly skewed due to the contribution of large, rare particles. This means that estimates of precision based on sample standard error or bootstrapping can under-state uncertainty whenever a sample happens to contain no large particles. To obtain defensible confidence limits we treat large-particle encounters as a Poisson process.

https://doi.org/10.5194/essd-2026-566
Preprint. Discussion started: 28 July 2026

2.9.4.1 Particle encounter

For an observed count of large particles n_l, one-sided Poisson confidence limits are

$$\lambda_{upper} = \frac{1}{2}\chi^2_{0.95,2(n_l+1)} \qquad \lambda_{lower} = \frac{1}{2}\chi^2_{0.05,2n_l}, \tag{5}$$

where $\chi^2_{p,\upsilon}$ is the p-quantile of a chi-square distribution with υ degrees of freedom. We then define the number of potential missed particles as $n_{miss} = \lambda_{upper} - n_l$ and the number of potential excess particles $n_{excess} = n_l - \lambda_{lower}$.

2.9.4.2 PSD Slope

The potential contributions to the mean and variance of b_{bl} of n_{miss} and n_{excess} are estimated assuming a power-law particle size distribution (PSD)

$n(D) = C\,D^{-b}$,

where C is a normalising constant, b is the PSD slope, ~~and~~ D is the equivalent-spherical diameter, and n(D) is the number of particles per unit diameter. For each value of b_{bl_raw}, the individual diameters of each particle with D≥200µm was obtained via

$$D = \sqrt{\frac{4}{\pi}\frac{b_{bl\_raw}\,V_i}{Q_{bb}}}, \tag{6}$$

where V_i is the volume sampled by a single measurement. Then, the fitted slope $\hat{b}$ is obtained with the Hill maximum-likelihood estimator applied to all particles >200µm

$$\hat{b} = \frac{N}{\sum_{i=1}^{N} ln(D_i/D_{min})},\ SE(\hat{b}) = \frac{\hat{b}-1}{\sqrt{N}} \tag{7}$$

Two independent constraints define the plausible interval for b:

1. Data-driven bound $\hat{b} \pm 1.96\,SE(\hat{b})$.
2. Literature bound ($b_{\mathrm{lit,min}} \le b \le b_{\mathrm{lit,max}}$), here taken as 3.3 – 4.5 for the open ocean.

The working bounds are the intersection of the two. These slopes are then inserted into the analytic moments of the PSD to obtain the additive mean and variance terms. The likely bounds of b were constrained as detailed below by a fit to the particle data themselves and by literature values:

$$\Delta\mathrm{A} = \frac{n\,\mu_A}{V_i} \tag{8}$$

$$\Delta\mathrm{Var_A} = \frac{n\,\mathrm{E}[A^2]}{V_i^2} - \frac{n^2\,\mu_A^2}{V_i^2} \tag{9}$$

where

$$\mu_A = \frac{\pi}{4}\,\frac{1-\mathrm{b}}{3-\mathrm{b}}\,\frac{D_{\mathrm{max}}^{3-b} - D_{\mathrm{min}}^{3-b}}{\mathrm{D}_{\mathrm{max}}^{1-\mathrm{b}} - \mathrm{D}_{\mathrm{min}}^{1-\mathrm{b}}} \tag{10}$$

https://doi.org/10.5194/essd-2026-566
Preprint. Discussion started: 28 July 2026

is the expected particle cross-sectional area, and

$$E[A^2] = \left(\frac{\pi}{4}\right)^2 \frac{1-b}{5-b} \frac{D_{max}^{5-b} - D_{min}^{5-b}}{D_{max}^{1-b} - D_{min}^{1-b}} \tag{11}$$

is the expected squared area. Here b is the PSD slope, n is either n_{miss} or n_{excess}, and $V_i \approx 10$ mL is the instrument sample volume. Because b_{bp} is proportional to particle cross-sectional area with efficiency Q_{bb}, the corresponding additions to b_{bp} and its variance are obtained with a fixed scale factor:

$$\Delta b_{bp} = Q_{bb}\, 10^{-6}\, \Delta A, \qquad \Delta \mathrm{Var}_{\mathrm{bbp}} = (Q_{bb}\, 10^{-6})^2\, \Delta \mathrm{Var}_{\mathrm{A}}. \tag{12}$$

These Δ terms are added to (for n_{miss}) or subtracted from (for n_{excess}) the observed mean and variance to yield the final upper and lower confidence bounds.

2.10 Global POC stocks and fluxes

The gridded climatologies described above have broad coverage but include gaps. Furthermore, particle size and flux estimates can have low precision where a single bin contains only a few measurements. Therefore, several additional steps were taken to estimate global and annual quantities (excluding the Arctic). First, bins containing <10 individual b_{bp} measurements were removed due to very low b_{bl} precision. Second, for each month and depth bin, spatial smoothing and local gap-filling was applied using a median filter with moving 3x3 grid cell window. Medians for windows containing <3 values were removed. Third, remaining spatial gaps were filled via linear interpolation by grid cell, treating 8° longitude and 4° latitude as equidistant. Global integrated POC fluxes for the open ocean were calculated using the gap-filled climatologies, multiplying the mean flux in each grid cell by the area of that grid cell with a bottom depth >1000 m.

2.11 Climatologies of other Argo parameters

For reference, the following other Argo parameters measured by the floats in this study were gridded in the same way: temperature, salinity, nitrate, pH, oxygen, and Chlorophyll a concentration. All adjusted parameters with Argo QC flags 1 or 2 are included, plus a separate variable for unadjusted temperature. Note that these climatologies are not appropriate for any purpose other than a reference to the POC concentrations and fluxes in this dataset, because they are derived only from floats measuring b_{bp} and not the full Argo dataset, and furthermore they have no quality assurance beyond the default Argo adjustments and flagging.

https://doi.org/10.5194/essd-2026-566
Preprint. Discussion started: 28 July 2026

3 Results

3.1 Data distribution

The monthly POC flux climatologies in this dataset are derived from data spread widely across all open ocean basins except the Arctic Ocean, but density and duration of coverage vary widely by region. The regions with the most years of coverage contributing to these climatologies are the Norwegian Sea, western Mediterranean, and Arabian Sea, with data from ≥10 years in a given 4° latitude by 8° longitude grid cell in at least some months of the year (Figure 6).

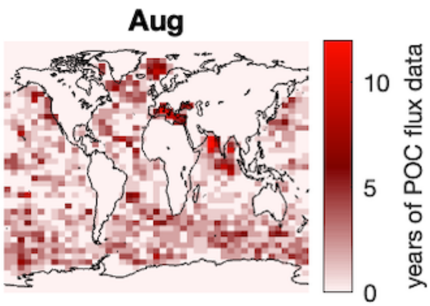

Figure 6. Number of years of August POC flux data per pixel between 100-150m, after quality control, out of the 16 years possible in this dataset (2010-2025).

3.2 Climatologies of near-surface POC, Chl, and particle size

For near-surface analysis, we examine the 10-50 m depth bin, because the top 10 m is more likely to contain variability in b_{bp} due to bubbles and variability in Chlorophyll a (Chla) due to difficulty in correcting non-photochemical quenching. In the near surface, climatologies of POC_{bb}, Chla, and $\overline{D}$ all follow similar first-order patterns (Figure 7-Figure 9), with strongest seasonality and highest peak values in the high latitudes. High-latitude peaks generally propagate poleward as the spring-summer progresses. Elevated Chla and $\overline{D}$ are also apparent in equatorial upwelling regions. The broad patterns in surface Chla are well-known due to satellite ocean colour measurements, with the major difference that, in our BGC-Argo dataset, coverage extends into the polar night and seasonal sea ice zones. $\overline{D}$ climatologies are noisier than those of the other parameters, due to the inherently lower precision of the method. However, some differences in climatological patterns can still be observed. In the northern hemisphere, $\overline{D}$ appears to peak in July in both the Norwegian Sea and the northeast Pacific, while Chla and POC_{bb} appear to peak earlier. In the southern hemisphere, the seasonal band of high $\overline{D}$ appears to be more concentrated poleward than the band of high Chla and POC_{bb}.

https://doi.org/10.5194/essd-2026-566
Preprint. Discussion started: 28 July 2026

Open Access Earth System Science Data Discussions

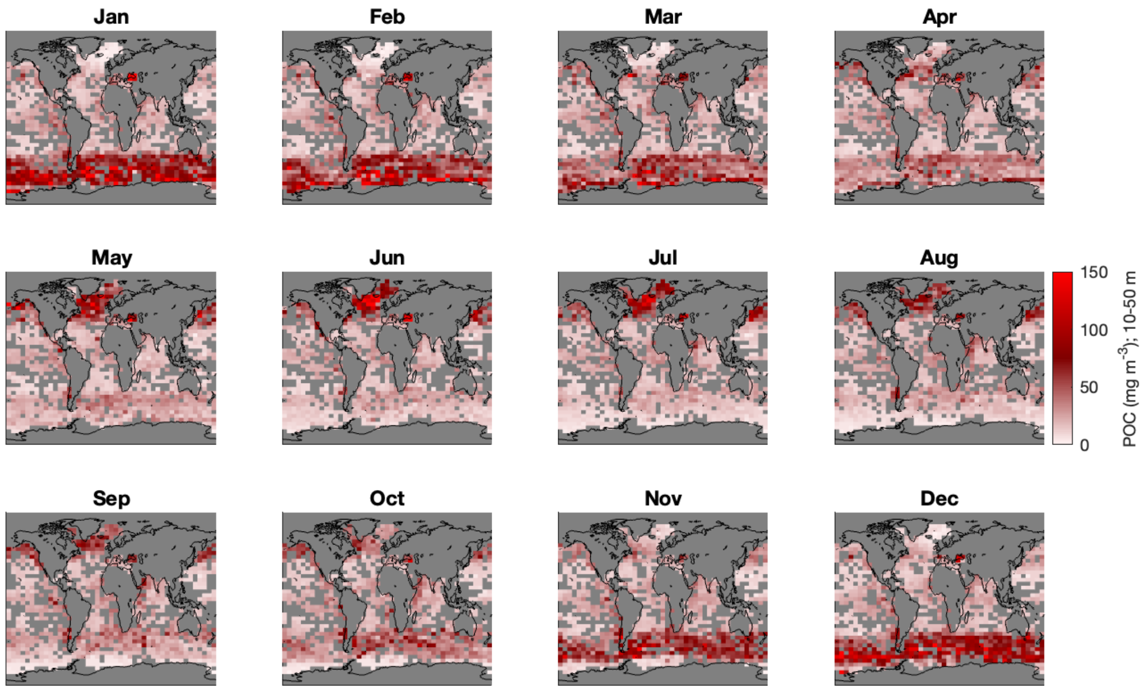

Figure 7. Climatological monthly mean POC_{bb} between 10-50 m.

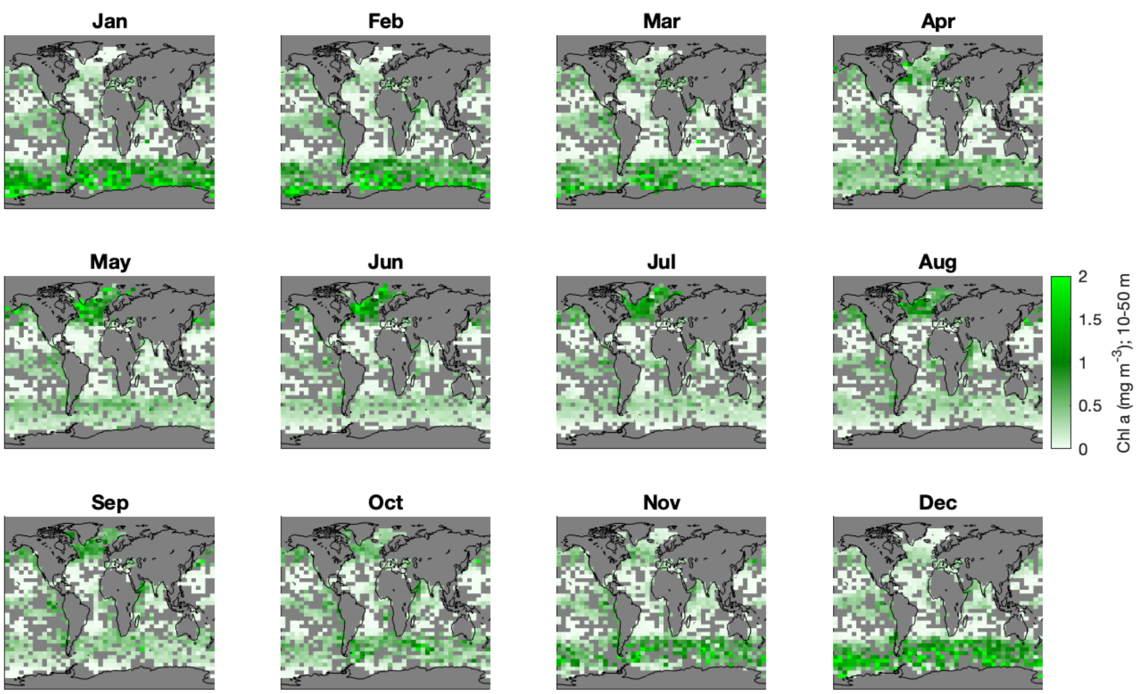

Figure 8. Climatological monthly mean in-situ fluorescence-derived Chl a between 10-50 m.

https://doi.org/10.5194/essd-2026-566
Preprint. Discussion started: 28 July 2026

Open Access Earth System Science Data Discussions

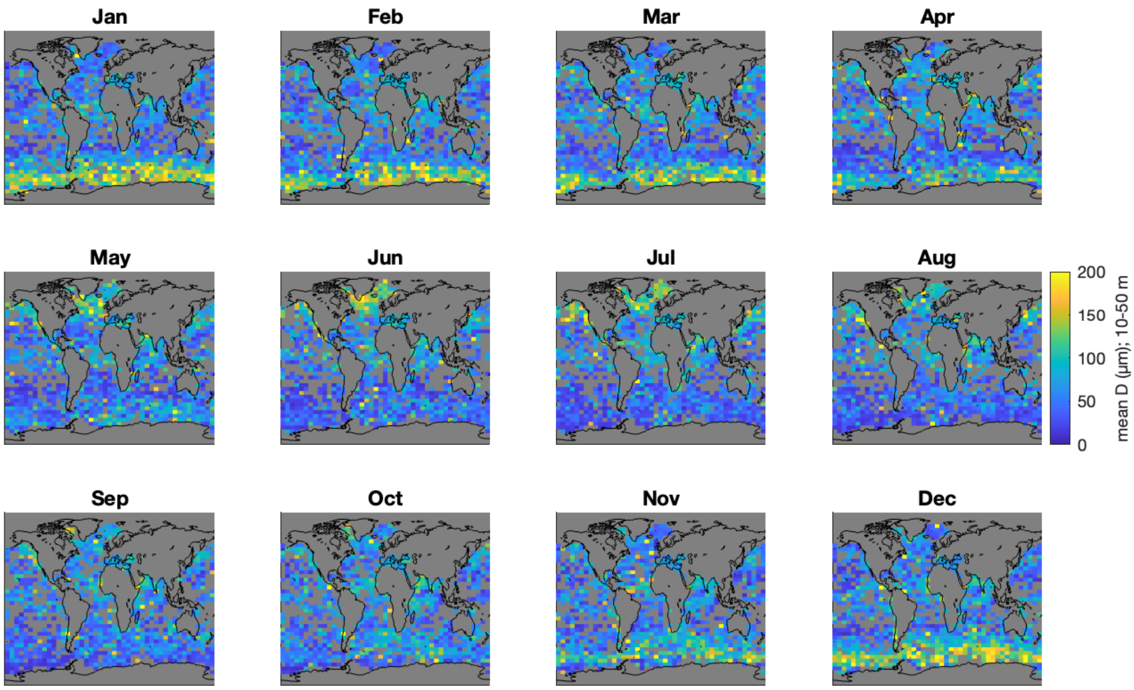

345 **Figure 9. Climatological monthly area-weighted mean particle diameter of particles <800µm between 10-50 m depth.**

3.3 Climatologies of mesopelagic POC flux

Climatologies of POC flux through the mesopelagic follow surface biomass to first order (Figure 10-Figure 11). Again, high-latitude seasonal bands of high flux propagate poleward in spring-summer. Elevated values in upwelling regions are less apparent, although these are also regions with lower coverage (Figure 6) and therefore noisier estimates. Mean climatologies by latitude band (Figure 12) accentuate some additional patterns shown in the climatological maps. Seasonality is strongest in all parameters in the highest latitudes. The highest monthly Chla peaks occur in the very highest latitudes (January between 70-80°S and June between 70-80°N), while the highest monthly peaks of surface POC and upper mesopelagic POC flux occur 10-20° closer to the equator. Seasonal peaks in $\overline{D}$, POC, and POC flux generally occur in the same month or the month after the peak in Chla, except between 70-80°S, where the peaks in near-surface particle size and POC export lag the Chla and POC peaks by two months.

https://doi.org/10.5194/essd-2026-566
Preprint. Discussion started: 28 July 2026

Open Access Earth System Science Data Discussions

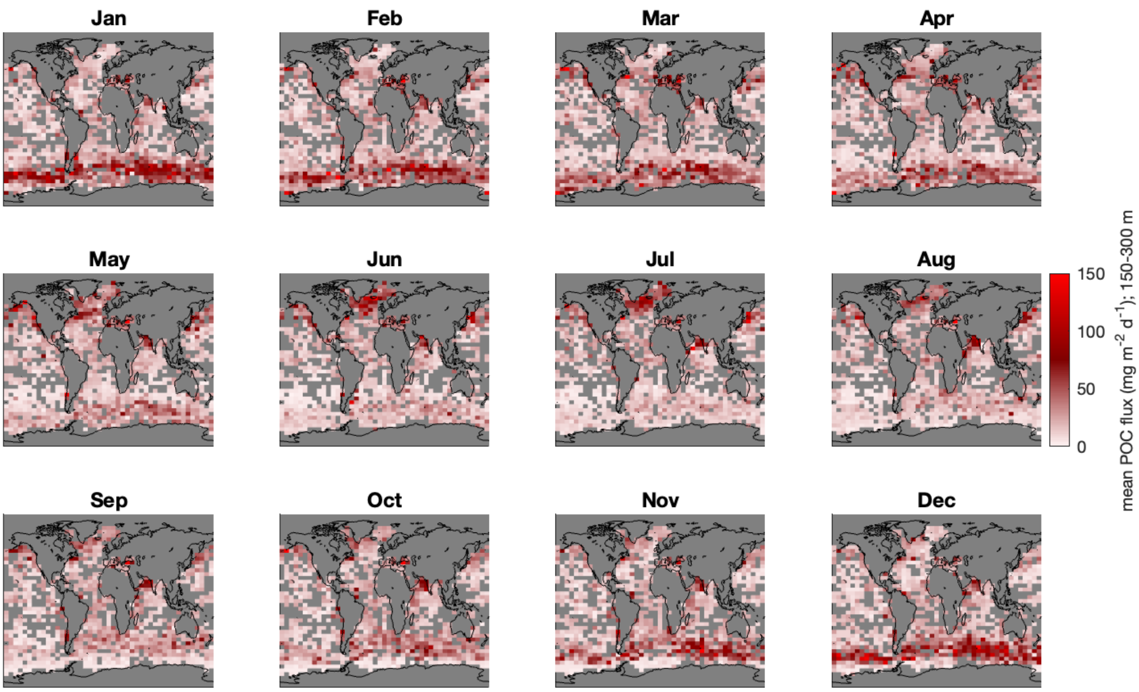

Figure 10. Monthly climatological mean sinking POC flux in the upper mesopelagic (150-300 m).

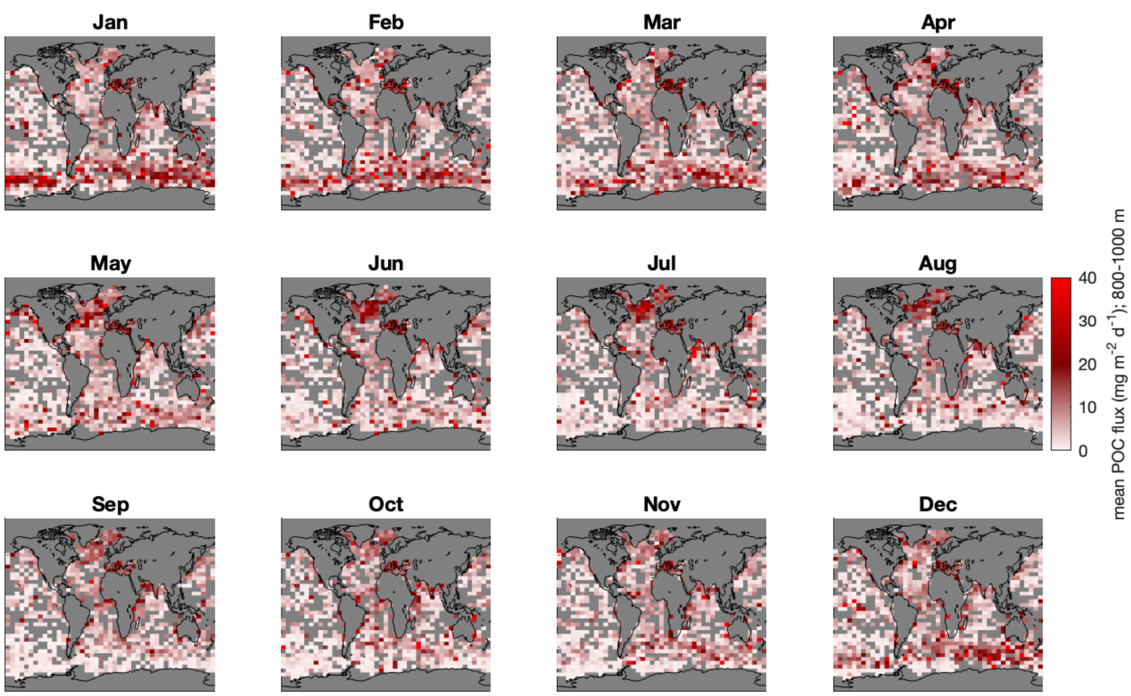

360 **Figure 11. Climatological monthly mean POC flux in the lower mesopelagic (800-975 m).**

https://doi.org/10.5194/essd-2026-566
Preprint. Discussion started: 28 July 2026

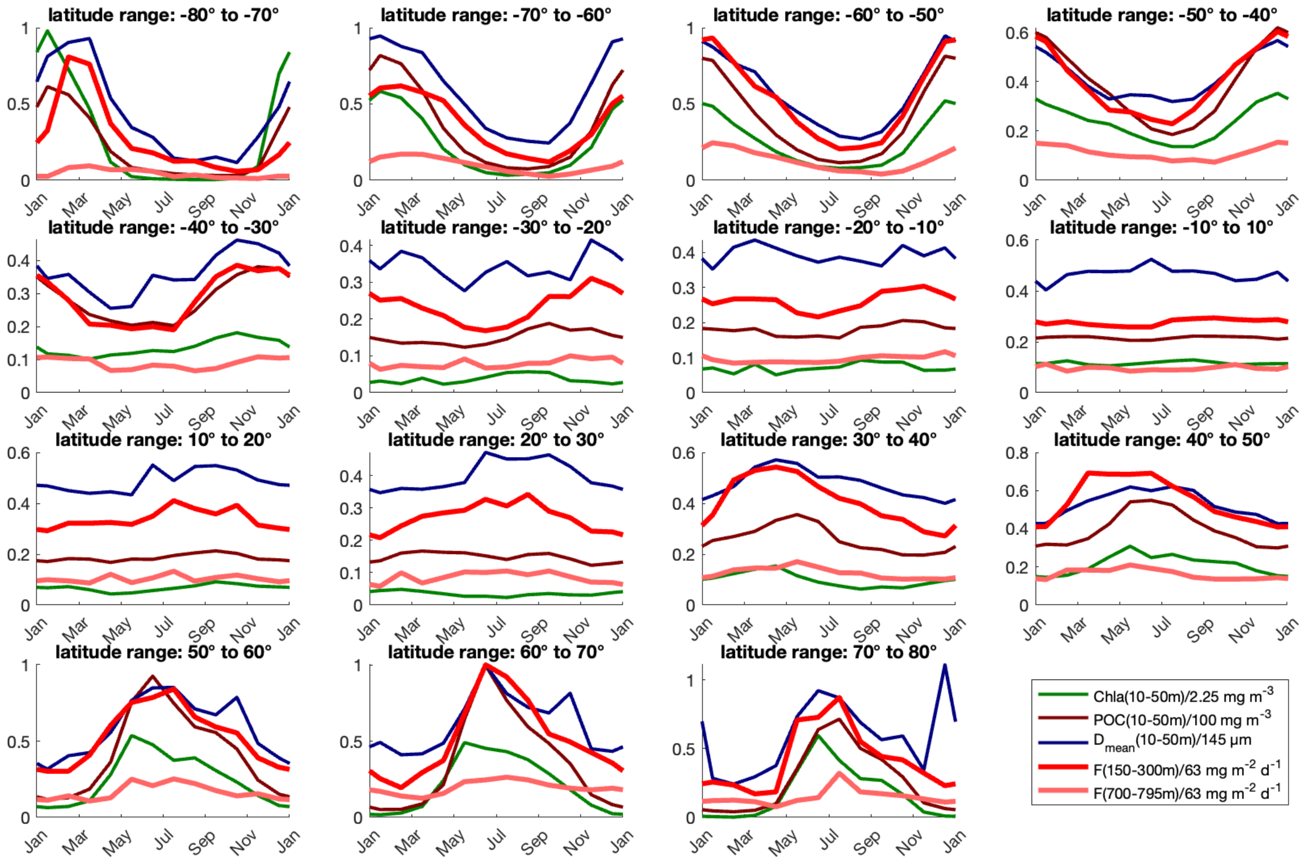

Figure 12. Seasonality of key parameters by latitude band: mean Chla (green), POC_{bb} (brown), and $\bar{D}$ (blue) between 10-50 m, mean POC flux (F) between 150-300 m (red), and mean POC flux (F) between 700-975 m (pink). Parameters are normalised as shown in the figure legend, each by the maximum across season and latitude, with the exception of lower mesopelagic POC flux, which maintains the same normalisation as upper mesopelagic POC flux to portray both depth attenuation and seasonality.

3.4 Global integrated flux

Global integrated sinking POC flux (and systematic uncertainty bounds), excluding the Arctic Ocean and continental shelves (bottom depth <1000 m), in this dataset is estimated to be 7.8 (4.1-13) Pg y^{-1} at 100 m, which is within the range of previous satellite data and inverse model-based estimates (Doney et al., 2024). The POC flux declines with depth to 0.49 (0.3-0.82) Pg y^{-1} at 1000 m, which is at the low end of previous estimates (Doney et al., 2024). The shape of global flux attenuation with depth approximately follows a power law or "Martin curve" between 175-950 m with a flux attenuation coefficient of -0.92±0.04 (Figure 13), close to the canonical value of -0.86. POC flux between 75-175 m deviates from this power law, with higher near-surface attenuation. Note that methodological uncertainties in this dataset are higher in this shallower range, due

https://doi.org/10.5194/essd-2026-566
Preprint. Discussion started: 28 July 2026

Open Access Earth System Science Data Discussions

to phytoplankton layers in the subtropics that can generate b_{bp} peaks that are misclassified as individual "large" particles (b_{bm} or b_{bl}).

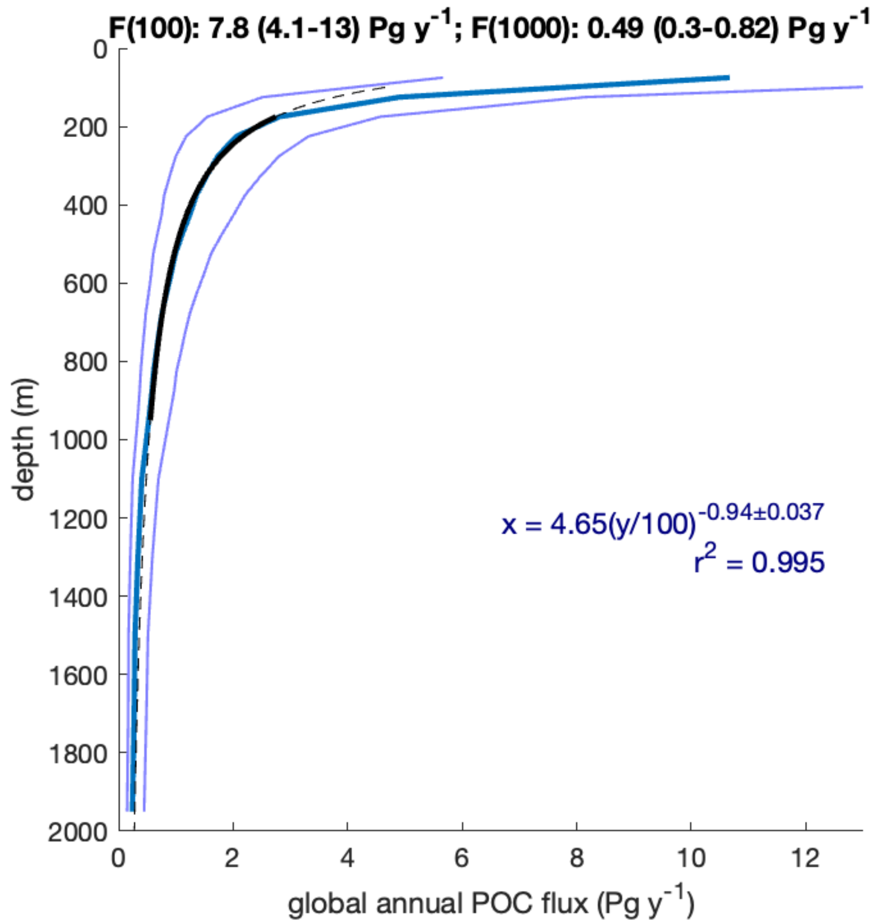

Figure 13. Profile of global integrated annual open-ocean sinking POC flux, excluding the Arctic Ocean and continental shelves shallower than 1000 m (thick blue line) and confidence bounds from propagation of systematic uncertainties (thin blue lines), shown with a power law fit to data between 175-950 m (solid black line), extrapolated to 100-2000 m (dashed black line). Power law exponent is -0.94±0.04. Global integrated POC flux (and uncertainty bounds), at key depths of 100 and 1000 m, are 7.8 (4.1-13) and 0.49 (0.3-0.82) Pg y^{-1}, respectively.

4 Discussion

4.1 Validation

Sinking POC flux estimates were validated using a global compilation of in-situ POC flux measurements made by sediment traps and the Thorium disequilibrium technique (Mouw et al., 2016), plus more recent sediment trap data from two long-term time-series stations: the Hawaiian Ocean Timeseries Site (HOT) and Bermuda Atlantic Timeseries Study (BATS). Both HOT

https://doi.org/10.5194/essd-2026-566
Preprint. Discussion started: 28 July 2026

and BATS timeseries were downloaded in November 2025 and span the years 1988-2024 (Johnson, 2025; Hawaii Ocean Time-Series, 2025).

4.1.1 Cleaning of validation dataset

The following outlier locations were removed from the (Mouw et al., 2016) validation dataset (hereafter M16) prior to calculation of validation statistics:

1. Data from K2 long-term timeseries from sediment traps deployed prior to the year 2010 were removed, as values had strong low bias relative to both more recent K2 data and other data from this latitude.
2. Data from most coastal DYFAMED site in the Mediterranean (43.4277°W, 7.2522°E), only 16 km from the coast (all prior to the year 2000).
3. Data from sediment traps with collection duration >60 days were removed to maintain better temporal matchups with monthly climatologies.

4.1.2 Global validation

Before matching with the GLOBESINK climatology, POC flux measurements from the M16 dataset made in the same month of the year by the same methodology at the same location were averaged together to reduce the influence of inter-annual variability. Then each M16 POC flux estimate was matched with the nearest GLOBESINK climatological grid cell in latitude, longitude, depth, and month of the year. Sediment trap measurements were matched with the midpoint of trap opening and closing dates, and estimates derived from thorium-234 disequilibrium were matched with the month eight days prior to the measurement, due to the residence time of 234^{Th} (Henson et al., 2012). If this grid cell contained a climatological POC flux estimate derived from ≥100 individual b_{bp} measurements, then the matchup was retained. Other matchups were rejected, due to low precision of GLOBESINK estimates.

A regression of GLOBESINK-M16 POC flux matchups shows good mean agreement at all depths, spanning two orders of magnitude (Figure 14). Correlation is moderately high (r^2=0.57), dominated by strong depth attenuation. Root mean square error (RMSE) is nevertheless high, corresponding to a factor of 3. This high RMSE can be partly attributed to the low precision of GLOBESINK estimates, partly attributed to inter-annual variability, and partly attributed to within-pixel variability, given the very large spatial bins of the GLOBESINK product. However, this RMSE also includes methodological uncertainties in both in-situ flux measurements and the GLOBESINK product. Methodological uncertainties in sediment trap measurements are well documented (Buesseler, 1991; Baker et al., 2020), so we focus here on sources of error in the GLOBESINK method. Principal sources of error are regional and seasonal variability in both the POC/bbp ratio and sinking speeds of particles, which, on a local scale, may substantially exceed the uncertainty bounds listed in Table 1, as these are uncertainties in the global mean values. The small-particle size class in particular corresponds to a very broad range of particle sizes, spanning from <1-200µm

https://doi.org/10.5194/essd-2026-566
Preprint. Discussion started: 28 July 2026

ESD. In addition, the GLOBESINK product excludes particles >800µm ESD, which can potentially dominate POC flux in specific times and places.

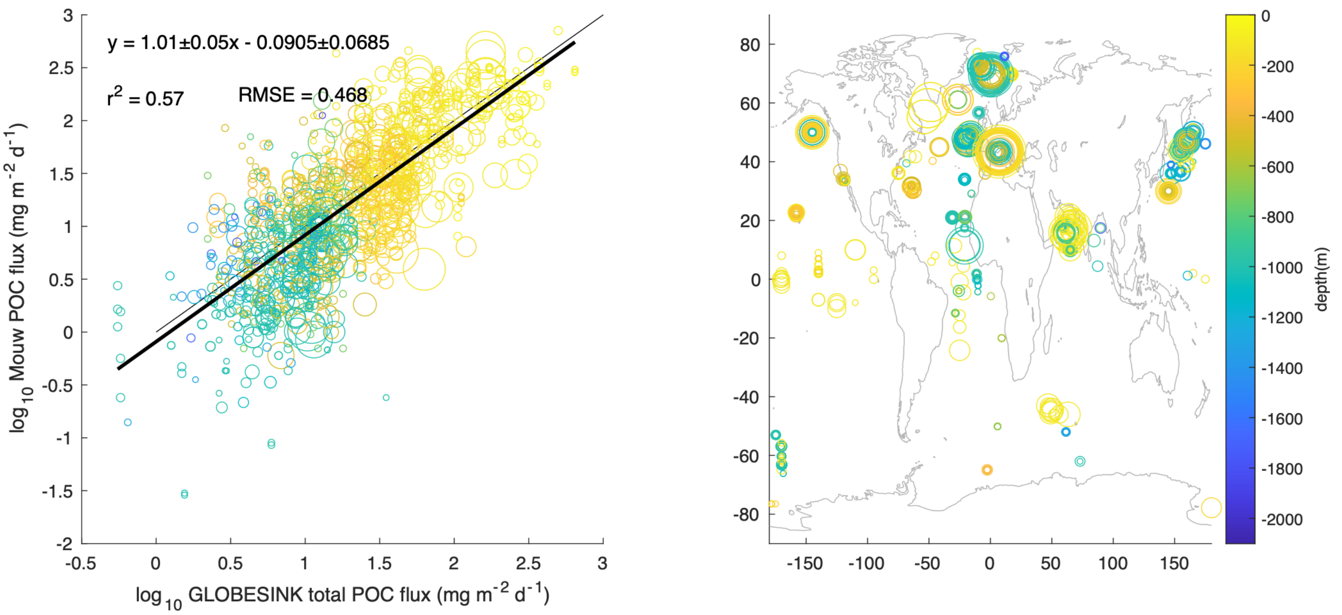

Figure 14. Validation of GLOBESINK total POC flux climatology against in-situ measurements from sediment traps and thorium-234 disequilibria from the Mouw et al. (2016) POC flux dataset. Left panel shows type I linear regression of $\log_{10}$(POC flux [mg m^{-2} d^{-1}]) from the GLOBESINK climatology (independent) vs the corresponding measurement from M16. Individual circles represent individual matched monthly estimates, with the 1:1 line (thin black line) and the regression line (thick black line) superimposed. Right panel shows a map of the location of all matching measurements used in the validation regression. In both panels colour scale shows measurement depth and area of circles is proportional to the number of b_{bp} measurements included in the GLOBESINK estimate.

4.1.3 Seasonal comparison with long-term timeseries sites

For most months of the year, GLOBESINK POC flux climatology agrees with monthly upper mesopelagic sediment trap data from the long-term timeseries stations HOT (Figure 15) and BATS (Figure 16), within the expected bounds of GLOBESINK precision and accuracy. The exception is January-March at BATS, when GLOBESINK systematically under-estimates sediment trap-derived flux throughout the upper mesopelagic. While it is possible that inter-annual or spatial variability contributes to this discrepancy, the degree of difference, especially at 300 m, suggests that the GLOBESINK method may be missing a seasonally important source of flux. This could potentially be a flux of particles >800µm ESD, which are explicitly excluded from the GLOBESINK estimates. Alternatively, this could be a flux of small particles sinking much faster than the GLOBESINK upper bound of 5 m d^{-1}, or particles with a much higher carbon density than average. This discrepancy highlights the limitations of the GLOBESINK method, which relies on bulk empirical relationships that minimise bias at global scale but may still result in important local biases.

https://doi.org/10.5194/essd-2026-566
Preprint. Discussion started: 28 July 2026

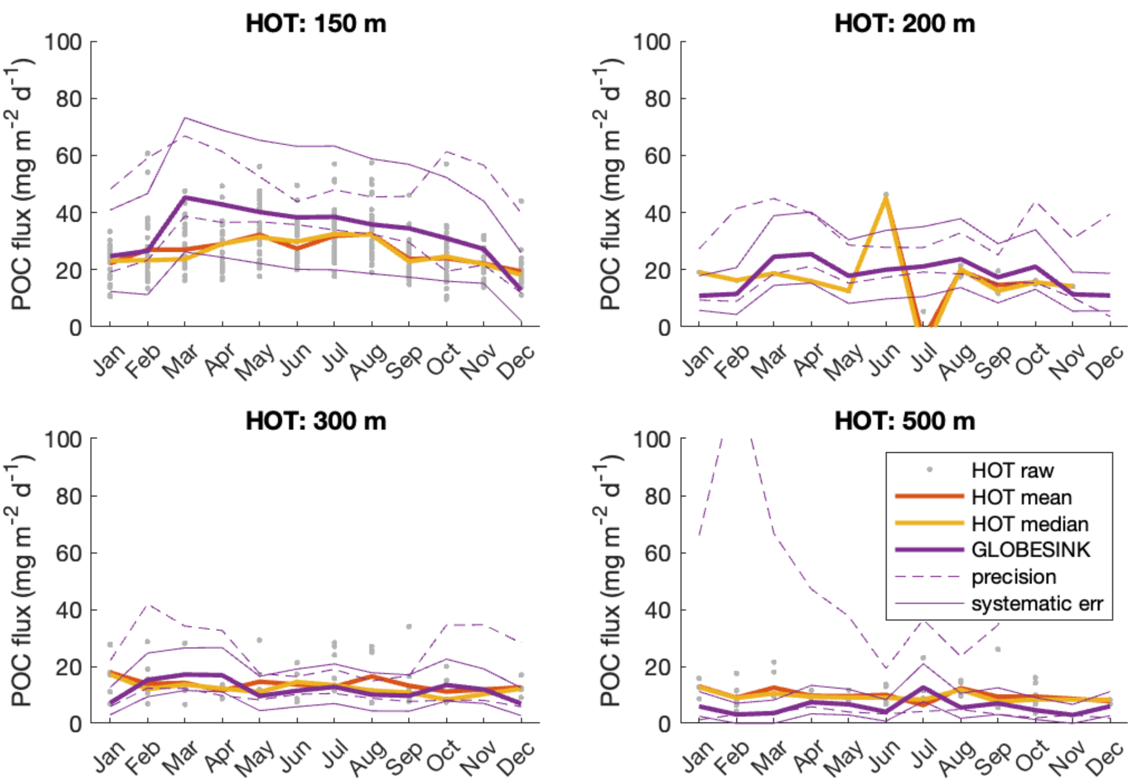

Figure 15. Comparison between POC flux estimates from Hawaii Ocean Timeseries monthly sediment trap data and the matchups from the GLOBESINK climatology, and associated precision and systematic errors described in Sections 2.9.3 and 2.9.4.

https://doi.org/10.5194/essd-2026-566
Preprint. Discussion started: 28 July 2026

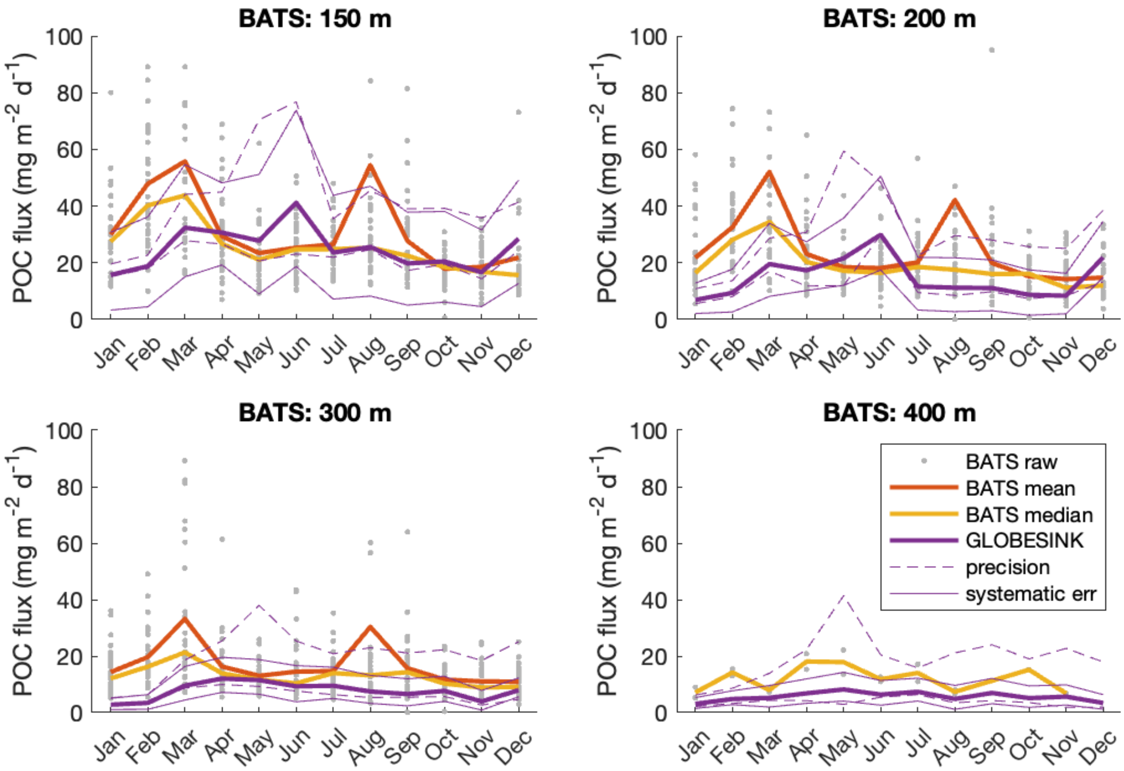

445 **Figure 16. Comparison between POC flux estimates from Bermuda Atlantic Timeseries Study monthly sediment trap data and the matchups from the GLOBESINK climatology, and associated precision and systematic errors described in Sections 2.9.3 and 2.9.4.**

4.1.4 Tuning of POC flux parameterisation

It is important to note that validation data should not be considered entirely independent, because the methodology for POC flux calculations was finalised after initial validation. Final fluxes should therefore be considered partially tuned, within bounds of literature parameterisations, to improve first-order quantitative agreement with validation datasets. The most impactful changes made to improve validation fit were 1) The decision to use a depth-dependent POC/b_{bp} ratio in the upper 100 m derived from reanalysis of (Cetinić et al., 2012), reducing an overall positive bias in mesopelagic flux, and 2) the decision to subtract a "refractory" pool, made after confirming that inclusion of the refractory pool in the GLOBESINK flux calculation caused a systematic over-estimation relative to sediment trap fluxes at depth and during the polar night.

https://doi.org/10.5194/essd-2026-566
Preprint. Discussion started: 28 July 2026

4.2 Guidelines for use of this dataset

The dataset published with this paper provides monthly climatological estimates of POC concentration, POC flux, mean particle diameter $\overline{D}$, and size-resolved particle concentrations, with associated precisions and uncertainties, alongside reference climatologies of temperature, salinity, Chla, dissolved O_2, NO_3, and pH.

The GLOBESINK POC flux dataset is best used as an indicative climatology, whose mean over broad time and space scales can be expected to agree to first order with sediment trap and thorium-234-based POC flux estimates, within the systematic uncertainty bounds provided. We therefore expect these estimates to be useful for large-scale carbon budgets and global biogeochemical model validation. However, on a local scale, in situ POC fluxes at any given place and time can be expected to regularly vary from the GLOBESINK climatology by either a factor of three (see RMSE in Figure 14), or the stated accuracy or precision of the specific GLOBESINK estimate, whichever is higher. This means that at local scale, quantification of systematic discrepancies between GLOBESINK POC fluxes and independent estimates that exceed the stated GLOBESINK uncertainties may be a useful tool for advancing process understanding beyond the simple size-based sinking model in this dataset. We also expect the GLOBESINK POC flux dataset to be a valuable tool for comparison with global and regional-scaled biogeochemical model results. Model outputs can be compared either directly with GLOBESINK fluxes or with POC content in the different size classes. We expect analyses of internal correlations between POC flux and other variables in the GLOBESINK data to be useful for enhancing understanding of empirical drivers of mesopelagic particle concentrations and fluxes in the global ocean.

The mean particle diameter climatology and large particle number concentrations have not been validated at global scale, so they are best used as a self-consistent, indicative climatologies of relative mean particle size and concentration. Note that the mean particle diameter $\overline{D}$ includes the influence of detrital particles such as aggregates and fecal pellets, so it therefore should not be used as an index of plankton size.

4.3 Plans for further dataset maintenance and development

As the global Biogeochemical Argo network continues to collect data, incorporation of these data into the GLOBESINK product promises to significantly enhance the dataset, improving precision of climatologies and starting to allow analysis of inter-annual variability. The authors aim to publish periodic updates to the GLOBESINK dataset. Future planned improvements also include quantitative validation and potential calibration of the particle size estimates.

Code and data availability

The GLOBESINK dataset is freely available in the Zenodo public repository at https://doi.org/10.5281/zenodo.19558504 (Briggs et al., 2026). Code to generate the dataset was written in Matlab and is available on request.

Earth System Science Data Discussions
Open Access

Author contributions

NB conceived the method, led funding acquisition, developed the software to generate and validate the GLOBESINK data product, and led writing of this manuscript. AF led the visual quality control of the GLOBESINK data and contributed to writing and editing of the manuscript. SH contributed to evaluation and calibration of the GLOBESINK dataset and writing and editing of the manuscript. HH contributed to the interpolated data product and reviewing of the manuscript.

Competing interests

The authors declare that they have no conflict of interest.

Acknowledgements

We are deeply grateful to all contributors to the international Argo programme and BGC Argo within it. The global year-round coverage of optical backscattering measurements, delivered in an open and standardised dataset, is an incredible achievement that has been the essential ingredient for this work. We would like to particularly highlight the contributions of the NSF-funded SOCCOM and GO-BGC projects, which together brought BGC Argo from regional to the true global coverage. We would also like to highlight the ERC-funded remOcean and REFINE projects, whose combination of scale and high vertical resolution have greatly improved the precision of the GLOBESINK product across wide swaths of the ocean, particularly in high-flux regions. The generative artificial intelligence tool ChatGPT was used to help with details of the precision calculations for selected GLOBESINK variables. This help included both coding and translating this code into written methods.

Financial support

This work was supported by the UK Natural Environment Research Council (NERC) GLOBESINK project (NE/X008657/1), the European Union Horizon 2020 project TechOceans (Grant Agreement No. 101000858), the NERC National Capability Single Centre Science Programme AtlantiS (NE/Y005589/1), and the European Union under grant agreement no. 101083922 (OceanICU) and UK Research and Innovation (UKRI) under the UK government's Horizon Europe funding guarantee (grant number 10054454, 10063673, 10064020, 10059241, 10079684, 10059012, 10048179).

5 References

Baker, C. A., Estapa, M. L., Iversen, M., Lampitt, R., and Buesseler, K.: Are all sediment traps created equal? An intercomparison study of carbon export methodologies at the PAP-SO site, Progress in Oceanography, 184, 102317, https://doi.org/10.1016/j.pocean.2020.102317, 2020.

Bishop, J. K. B., Wood, T. J., Davis, R. E., and Sherman, J. T.: Robotic Observations of Enhanced Carbon Biomass and Export at 55°S During SOFeX, Science, 304, 417-420, doi:10.1126/science.1087717, 2004.

https://doi.org/10.5194/essd-2026-566
Preprint. Discussion started: 28 July 2026

Briggs, N., Dall'Olmo, G., and Claustre, H.: Major role of particle fragmentation in regulating biological sequestration of CO2 by the oceans, Science, 367, 791-793, 10.1126/science.aay1790, 2020.

Briggs, N., Henson, S., Flohr, A., and Hilder, H.: GLOBESINK monthly POC flux and particle size climatology, Zenodo [dataset], 10.5281/ZENODO.19558504, 2026.

Briggs, N., Perry, M. J., Cetinić, I., Lee, C., D'Asaro, E., Gray, A. M., and Rehm, E.: High-resolution observations of aggregate flux during a sub-polar North Atlantic spring bloom, Deep Sea Research Part I: Oceanographic Research Papers, 58, 1031-1039, 10.1016/j.dsr.2011.07.007, 2011.

Briggs, N. T., Slade, W. H., Boss, E., and Perry, M. J.: Method for estimating mean particle size from high-frequency fluctuations in beam attenuation or scattering measurements, Appl Opt, 52, 6710-6725, 10.1364/AO.52.006710, 2013.

Buesseler, K. O.: Do upper-ocean sediment traps provide an accurate record of particle flux?, Nature, 353, 420-423, 10.1038/353420a0, 1991.

Buesseler, K. O. and Boyd, P. W.: Shedding light on processes that control particle export and flux attenuation in the twilight zone of the open ocean, Limnology and Oceanography, 54, 1210-1232, https://doi.org/10.4319/lo.2009.54.4.1210, 2009.

Cael, B. B., Cavan, E. L., and Britten, G. L.: Reconciling the Size-Dependence of Marine Particle Sinking Speed, Geophysical Research Letters, 48, 10.1029/2020gl091771, 2021.

Canadell, J. G., Monteiro, P. M. S., Costa, M. H., Cotrim da Cunha, L., Cox, P. M., Eliseev, A. V., Henson, S., Ishii, M., Jaccard, S., Koven, C., Lohila, A., Patra, P. K., Piao, S., Rogelj, J., Syampungani, S., Zaehle, S., Zickfeld, K., and Suntharalingam, P.: Global Carbon and other Biogeochemical Cycles and Feedbacks, in: Climate Change 2021: The Physical Science Basis, edited by: Masson-Delmotte, V., Zhai, P., Pirani, A., Connors, S. L., Péan, C., Berger, S., Caud, N., Chen, Y., Goldfarb, L., Gomis, M. I., Huang, M., Leitzell, K., Lonnoy, E., Matthews, J. B. R., Maycock, T. K., Waterfield, T., Yelekçi, O., Yu, R., and Zhou, B., Cambridge University Press, Cambridge, United Kingdom and New York, NY, USA, 673-816, 10.1017/9781009157896.007, 2021.

Cetinić, I., Perry, M. J., Briggs, N. T., Kallin, E., D'Asaro, E. A., and Lee, C. M.: Particulate organic carbon and inherent optical properties during 2008 North Atlantic Bloom Experiment, Journal of Geophysical Research: Oceans, 117, 2012.

Claustre, H., Johnson, K. S., and Takeshita, Y.: Observing the Global Ocean with Biogeochemical-Argo, Ann Rev Mar Sci, 12, 23-48, 10.1146/annurev-marine-010419-010956, 2020.

Doney, S. C., Mitchell, K. A., Henson, S. A., Cavan, E., DeVries, T., Gruber, N., Hauck, J., Mouw, C. B., Müller, J. D., and Primeau, F. W.: Observational and Numerical Modeling Constraints on the Global Ocean Biological Carbon Pump, Global Biogeochemical Cycles, 38, e2024GB008156, https://doi.org/10.1029/2024GB008156, 2024.

Estapa, M. L., Feen, M. L., and Breves, E.: Direct Observations of Biological Carbon Export From Profiling Floats in the Subtropical North Atlantic, Global Biogeochemical Cycles, 33, 282-300, 10.1029/2018gb006098, 2019.

Guidi, L., Legendre, L., Reygondeau, G., Uitz, J., Stemmann, L., and Henson, S. A.: A new look at ocean carbon remineralization for estimating deepwater sequestration, Global Biogeochemical Cycles, 29, 1044-1059, 10.1002/2014gb005063, 2015.

Haentjens, N., Della Penna, A., Briggs, N., Karp-Boss, L., Gaube, P., Claustre, H., and Boss, E.: Detecting Mesopelagic Organisms Using Biogeochemical-Argo Floats, Geophys Res Lett, 47, e2019GL086088, 10.1029/2019GL086088, 2020.

Hawaii Ocean Time-series, P.: Particle flux time-series (150–500 m) [dataset], 2025.

Henson, S. A., Sanders, R., and Madsen, E.: Global patterns in efficiency of particulate organic carbon export and transfer to the deep ocean, Global Biogeochemical Cycles, 26, n/a-n/a, 10.1029/2011gb004099, 2012.

Henson, S. A., Briggs, N., Carvalho, F., Manno, C., Mignot, A., and Thomalla, S.: A seasonal transition in biological carbon pump efficiency in the northern Scotia Sea, Southern Ocean, Deep Sea Research Part II: Topical Studies in Oceanography, 208, 10.1016/j.dsr2.2023.105274, 2023.

Henson, S. A., Sanders, R., Madsen, E., Morris, P. J., Le Moigne, F., and Quartly, G. D.: A reduced estimate of the strength of the ocean's biological carbon pump, Geophysical Research Letters, 38, n/a-n/a, 10.1029/2011gl046735, 2011.

Iken, K., Brey, T., Wand, U., Voigt, J., and Junghans, P.: Food web structure of the benthic community at the Porcupine Abyssal Plain (NE Atlantic): a stable isotope analysis, Progress in Oceanography, 50, 383-405, https://doi.org/10.1016/S0079-6611(01)00062-3, 2001.

Johnson, K. S., Plant, J. N., Coletti, L. J., Jannasch, H. W., Sakamoto, C. M., Riser, S. C., Swift, D. D., Williams, N. L., Boss, E., Haëntjens, N., Talley, L. D., and Sarmiento, J. L.: Biogeochemical sensor performance in the SOCCOM profiling float array, Journal of Geophysical Research: Oceans, 122, 6416-6436, 10.1002/2017jc012838, 2017.

https://doi.org/10.5194/essd-2026-566
Preprint. Discussion started: 28 July 2026

Johnson, R. J., Bates, N., Lomas, M. W., Steinberg, D. K., Derbyshire, L., Hayden, M. G., Lomas, D., Lethaby, P. J., Lopez, P. Z., May, R., Smith, D., Stuart, E., Enright, M.: Determination of carbon, nitrogen, and phosphorus content in sinking particles at the Bermuda Atlantic Time-series Study (BATS) site from December 1988 to December 2024 using a Particle Interceptor Trap System (PITS). ((Version 6) Version Date 2025-06-24) [dataset], doi:10.26008/1912/bco-dmo.894099.6, 2025.

Lima, I. D., Lam, P. J., and Doney, S. C.: Dynamics of particulate organic carbon flux in a global ocean model, Biogeosciences, 11, 1177-1198, 10.5194/bg-11-1177-2014, 2014.

Mouw, C. B., Barnett, A., McKinley, G. A., Gloege, L., and Pilcher, D.: Global ocean particulate organic carbon flux merged with satellite parameters, Earth Syst. Sci. Data, 8, 531-541, 10.5194/essd-8-531-2016, 2016.

Roemmich, D., Alford, M. H., Claustre, H., Johnson, K., King, B., Moum, J., Oke, P., Owens, W. B., Pouliquen, S., Purkey, S., Scanderbeg, M., Suga, T., Wijffels, S., Zilberman, N., Bakker, D., Baringer, M., Belbeoch, M., Bittig, H. C., Boss, E., Calil, P., Carse, F., Carval, T., Chai, F., Conchubhair, D. Ó., d'Ortenzio, F., Dall'Olmo, G., Desbruyeres, D., Fennel, K., Fer, I., Ferrari, R., Forget, G., Freeland, H., Fujiki, T., Gehlen, M., Greenan, B., Hallberg, R., Hibiya, T., Hosoda, S., Jayne, S., Jochum, M., Johnson, G. C., Kang, K., Kolodziejczyk, N., Körtzinger, A., Traon, P.-Y. L., Lenn, Y.-D., Maze, G., Mork, K. A., Morris, T., Nagai, T., Nash, J., Garabato, A. N., Olsen, A., Pattabhi, R. R., Prakash, S., Riser, S., Schmechtig, C., Schmid, C., Shroyer, E., Sterl, A., Sutton, P., Talley, L., Tanhua, T., Thierry, V., Thomalla, S., Toole, J., Troisi, A., Trull, T. W., Turton, J., Velez-Belchi, P. J., Walczowski, W., Wang, H., Wanninkhof, R., Waterhouse, A. F., Waterman, S., Watson, A., Wilson, C., Wong, A. P. S., Xu, J., and Yasuda, I.: On the Future of Argo: A Global, Full-Depth, Multi-Disciplinary Array, Frontiers in Marine Science, 6, 10.3389/fmars.2019.00439, 2019.

Romero-Romero, S., Miller, L. C., Black, J. A., Popp, B. N., and Drazen, J. C.: Abyssal deposit feeders are secondary consumers of detritus and rely on nutrition derived from microbial communities in their guts, Scientific Reports, 11, 12594, 10.1038/s41598-021-91927-4, 2021.

Siegel, D. A., Buesseler, K. O., Doney, S. C., Sailley, S. F., Behrenfeld, M. J., and Boyd, P. W.: Global assessment of ocean carbon export by combining satellite observations and food-web models, Global Biogeochemical Cycles, 28, 181-196, 10.1002/2013gb004743, 2014.

Stramski, D., Reynolds, R. A., Babin, M., Kaczmarek, S., Lewis, M. R., Röttgers, R., Sciandra, A., Stramska, M., Twardowski, M. S., Franz, B. A., and Claustre, H.: Relationships between the surface concentration of particulate organic carbon and optical properties in the eastern South Pacific and eastern Atlantic Oceans, Biogeosciences, 5, 171-201, 10.5194/bg-5-171-2008, 2008.

Tjiputra, J. F., Couespel, D., and Sanders, R.: Marine ecosystem role in setting up preindustrial and future climate, Nature Communications, 16, 2206, 10.1038/s41467-025-57371-y, 2025.

Usbeck, R., Schlitzer, R., Fischer, G., and Wefer, G.: Particle fluxes in the ocean: comparison of sediment trap data with results from inverse modeling, Journal of Marine Systems, 39, 167-183, https://doi.org/10.1016/S0924-7963(03)00029-0, 2003.